*Bangladesh Journal of Physics, Vol. **27**, Issue 1, pp. 69–80, June 2020*

EFFECTS OF PUMP-PULSE WIDTH AND TEMPERATURE ON EXPERIMENTAL BRILLOUIN GAIN SPECTRUM OBTAINED FROM BRILLOUIN OPTICAL TIME-DOMAIN ANALYSIS SENSORS

ABUL KALAM AZAD

Department of Electrical and Electronic Engineering, University of Dhaka, Dhaka-1000, Bangladesh

**Corresponding author: E-mail: azad@du.ac.bd*

Received on 12.07.2020, Revised received on 18.08.2020, Accepted for Publication on 20.08.2020

DOI: https://doi.org/10.3329/bjphy.v27i1.49727

ABSTRACT

In this paper, the characteristics of Brillouin gain spectrum (BGS) obtained from a Brillouin optical time-domain analysis (BOTDA) sensor are investigated and analyzed experimentally. The measured BGSs obtained for various pump-pulse widths and temperatures are fitted with different spectrum profiles using nonlinear least-squares curve fitting technique. The fitting performances of used profiles are presented and analyzed. Based on such performances, the proper spectrum profile to be used in the fitting process is determined and used to extract key parameters of the measured BGSs accurately. The variations of such key parameters with pump-pulse widths and temperatures are also investigated and analyzed. The results reveal that pump-pulse widths and temperatures have significant effects on the extracted key parameters of the measured BGSs obtained from BOTDA sensors.

Keywords: Stimulated Brillouin scattering, Fiber optic sensors, Brillouin gain spectrum, Least-squares curve fitting, Pseudo-Voigt profile.

1. INTRODUCTION

Fiber-optic sensors effectively substitute traditional electrical sensors to measure a wide variety of physical parameters in a distributed manner [1-4]. Among various fiber-optic sensors, stimulated Brillouin scattering (SBS) based Brillouin optical time-domain analysis (BOTDA) sensors have been intensively studied due to their ability to monitor temperature or stain precisely with high resolution over several tens of kilometres long fiber [4-7]. In such BOTDA sensors, an intense pulsed pump signal and a counter-propagating weak continuous-wave (CW) probe signal interact in the fiber through the process of SBS [4,5]. As a result, acoustic phonons are generated which scatter photons from the pump-pulse to amplify the weak probe signal. The power gained by the probe signal along the fiber under test (FUT) is recorded in time-domain for a given pump-probe frequency offset. By step-by-step scanning the pump-probe frequency offsets, the measured Brillouin gain spectrum (BGS) at each fiber location is retrieved as a function of frequency [3,4].

The measured BGS is ideally modeled by its three key parameters, i.e., the peak Brillouin gain (PBG), the central frequency which is also called Brillouin frequency shift (BFS), and the full width at the half-maximum (FWHM) [4,8]. These parameters are usually extracted by using curve fitting technique in which a measured BGS is fitted with a given spectrum profile. Once the fitting process is over, the parameters PBG, BFS and FWHM of the measured BGS is assumed to be that of the fitted curve [8,9].

The measured BGS obtained from BOTDA sensors results from the convolution operation between the pump-pulse spectrum and the inherent Lorentzian profile of the natural gain spectrum [9,10]. As a result, the shape of the BGS becomes mostly Lorentzian having narrower FWHM when sufficient longer pump-pulse width (i.e., narrower spectrum) compared to the phonon life-time of ~10 ns is used. On the contrary, its shape is mostly Gaussian having wider FWHM when shorter pump-pulse (i.e., broader spectrum) on the order of phonon life-time is used in BOTDA sensors to improve the spatial resolution. Thus, the fitting of measured BGS with an arbitrary chosen profile may provide lower fitting performance depending on the pump-pulse width. However, the convolution operation always provides a shape of the measured BGS to be in between a Lorentzian profile and a Gaussian profile which is referred to as a Voigt profile [11,12]. The fitting of measured BGS with Voigt profile involves convolution operation which is computationally complex and thus relatively slower. To reduce such complexity, the Voigt profile can be well-approximated by pseudo-Voigt profile which is solely the weighted summation of Lorentzian and Gaussian profiles [12,13]. As a result, the fitting of measured BGS obtained using pump-pulses of different widths with a pseudo-Voigt profile should provide reasonably better fitting performance as compared to that with a Lorentzian or a Gaussian profile.

Recently, principal component analysis and neural network based techniques have been proposed and demonstrated for processing BOTDA-measured BGSs along the FUT [14-18]. In the modeling of such techniques, the Lorentzian profile is frequently used for simulating the reference spectrum. However, the shape of measured BGSs depends on the experimental conditions and diverges greatly from Lorentzian to Gaussian profile depending on the pump-pulse width used to set the spatial resolution of the sensor [8,13]. The temperature applied on the FUT also affects the shape of the measured BGSs [8]. This mismatch between the measured BGSs and the simulated reference spectrum also affects the measurement accuracy of such signal processing techniques. As a result, the experimental conditions (e.g., pump-pulse and temperature) should be considered while simulating the reference spectrum to make such techniques more rational for accurate measurement. To find a proper spectrum profile, it is thus vital to study the effects of pump-pulse width and temperature on the measured BGS. In this study, the key parameters of measured BGSs obtained for various pump-pulse widths and temperatures are extracted systematically using nonlinear curve fitting technique. The effects of pump-pulse width and temperature on the measured BGS obtained from the BOTDA experiment are also investigated and analyzed in detail.

2. EXPERIMENTAL SETUP OF THE BOTDA SENSOR

The experimental setup of the BOTDA sensor is shown in Fig. 1. In the setup, the coupler splits the output of a tunable laser operating at 1550 nm and provides CW waves for the upper and lower branches. The polarization states of the CW waves in two branches are adjusted by the polarization controllers PC1 and PC2. To generate pump-pulses, the CW wave in the upper branch is modulated by a pulse-pattern-generator (PPG) driven electro-optic modulator (EOM1). The pump-pulses are then passed through an erbium-doped fiber amplifier (EDFA) so that their peak-power can be boosted up to the desired level. Next, a band pass filter (BPF) is used to remove the amplified spontaneous emission (ASE) noise introduced by EDFA. Finally, the polarization scrambler (PS) helps to randomize the polarization states of pump-pulses in the upper branch.

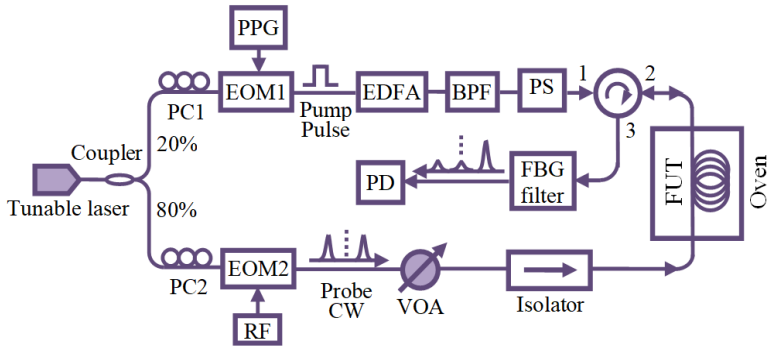

Fig. 1. The Experimental setup of the BOTDA sensor.

In the lower branch of the experimental setup, another electro-optic modulator (EOM2) driven by a radio-frequency (RF) signal generator modulates the CW wave for generating double-sideband suppressed-carrier probe signal. The EOM2 is followed by a variable optical attenuator (VOA) whose function is to control the power of the CW probe signal and then an isolator is employed to block the signal transmission towards this lower branch from the FUT.

Due to the interaction of pump and probe signals through SBS, the probe signal in the FUT is amplified. The unwanted higher frequency sideband of the amplified probe signal is filtered out by using a fiber Bragg grating (FBG) filter before being detected by the photodetector (PD). Then, the pump-probe frequency offset is scanned subsequently around the BFS at a particular frequency step and the time-domain traces are used to reconstruct the BGSs along the FUT.

3. OPERATING PRINCIPLE OF CURVE FITTING TECHNIQUE

The key parameters of the measured BGS are extracted by using nonlinear least-squares curve fitting technique. To study the spectrum shape, the measured BGS obtained for a particular pump-pulse width and temperature is fitted with different spectrum profiles, i.e., the Lorentzian (g_L), the Gaussian (g_G) and the pseudo-Voigt (g_{pV}) profiles given by Eq. (1) – Eq. (3), respectively [15,19].

$$g_L(\upsilon) = \frac{g_B}{1+4[(\upsilon-\upsilon_B)/(\Delta\upsilon_B)]^2} \tag{1}$$

$$g_G(\upsilon) = g_B \exp\left[-4\ln 2\left((\upsilon-\upsilon_B)/\Delta\upsilon_B\right)^2\right] \tag{2}$$

$$g_{pV}(\upsilon) = L\left\{\frac{g_B}{1+4[(\upsilon-\upsilon_B)/(\Delta\upsilon_B)]^2}\right\} + (1-L)\left\{g_B \exp\left[-4\ln 2\left((\upsilon-\upsilon_B)/\Delta\upsilon_B\right)^2\right]\right\} \tag{3}$$

In Eq. (1) – Eq. (3), g_B is the PBG, υ_B is the BFS and $\Delta\upsilon_B$ is the FWHM of a given spectrum profile. The pseudo-Voigt profile given by Eq. (3) is a linear combination of Lorentzian and Gaussian profiles given by Eq. (1) and Eq. (2), respectively and the Lorentzian proportion L in Eq. (3) is the proportion taken by Lorentzian profile in a pseudo-Voigt profile. The pseudo-Voigt profile given by Eq. (3) becomes a perfect Lorentzian profile and a perfect Gaussian profile for L values of 1 and 0, respectively. Hereafter, the fittings of the measured BGS with Lorentzian, Gaussian and pseudo-

Voigt profiles will be termed as Lorentzian curve fitting (LCF), Gaussian curve fitting (GCF) and pseudo-Voigt curve fitting (pVCF), respectively.

In LCF, GCF and pVCF, the measured BGS for a particular pump-pulse width and temperature is fitted with Lorentzian, Gaussian and pseudo-Voigt profiles given by Eq. (1) - Eq. (3), respectively and the least-squares error is minimized using the widely used Levenberg-Marquardt algorithm [20]. The fitting process using this algorithm starts with the initial guess of a vector **p** containing the model parameters of the given spectrum profile. The vector **p** is updated iteratively for N data points of the measured BGS such that the error function [15] given by Eq. (4) is minimized. The

$$E(\mathbf{p}) = \sum_{i=1}^{N} \left[g(\upsilon_i) - g(\upsilon_i, \mathbf{p}) \right]^2 \tag{4}$$

vector **p** in Eq. (4) is usually chosen from the underlying curve and initialized as $\mathbf{p} = [g_B, \nu_B, \Delta\nu_B]$ for both LCF and GCF, and $\mathbf{p} = [L, g_B, \nu_B, \Delta\nu_B]$ for pVCF. Once the fitting process is over, the fitted parameters in the vector **p** are assumed to be that of the measured BGS.

4. EXPERIMENTAL RESULTS AND DISCUSSION

4.1 Acquisition of measured BGSs from the BOTDA sensor

For the acquisition of measured BGSs, the whole span of a 200 m long FUT is heated inside an oven each time at a constant temperature adopting a given pump-pulse width in the BOTDA setup shown in Fig. 1. For instance, the distributions of measured BGSs along the FUT at 25°C obtained using the frequency range from 10.75 GHz to 10.95 GHz for different pump-pulse widths of 10 ns, 15 ns, 30 ns and 100 ns are shown in Fig. 2. It is observed from Fig. 2 that the BGSs along the

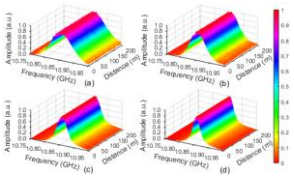

Fig. 2. Distributions of measured BGSs along the FUT at 25°C for different pump-pulse widths of (a) 10 ns, (b) 15 ns, (c) 30 ns and (d) 100 ns.

FUT are widest for the pump-pulse width of 10 ns, the shortest pump-pulse used in this study. As the width of pump-pulse increases, the BGSs turn out to be significantly narrower and become narrowest for 100 ns pump-pulse which is the longest pump-pulse used in this study.

In this demonstration, the measured BGSs along the FUT at each temperature and pump-pulse width are obtained using sampling rate of 250 Mega-symbols/second, i.e., sampling interval of 0.4 m along the FUT. During the acquisition of BGSs, 2000 time-domain traces are averaged to obtain a single trace at a particular pump-probe frequency offset so that the signal-to-noise ratio (SNR) of the measured BGSs can be enhanced to a satisfactory level. The measured BGSs are obtained for a frequency range of 200 MHz around their peaks with a frequency step of 1 MHz. The BGSs acquired from the BOTDA setup is normalized to make the peak gain of each BGS equal to 1. For a given pump-pulse width and temperature, the normalized BGSs along the FUT are ideally identical. Practically, the BGSs are almost similar with a little variation caused by random noise. Thus, all the BGSs along the FUT obtained at a particular pump-pulse width and temperature are averaged to obtain a single BGS representing that particular pump-pulse width and temperature. Hereafter, the averaged BGS will be termed as measured BGS. In this study, the measured BGSs are acquired at three different oven temperatures of 25°C, 50°C and 75°C each time by adopting different pump-pulse widths ranging from 10 ns to 100 ns. The measured BGSs are also obtained for two different pump-pulse widths of 20 ns and 70 ns each time at different temperatures ranging from 25°C to 75°C. Since, the BFS of the BGS depends linearly on the change of temperature [4,8], the measured BGSs at 25°C, 50°C and 75°C are obtained for different frequency ranges starting from 10.75 GHz to 10.95 GHz, 10.78 GHz to 10.98 GHz and 10.80 GHz to 11.00 GHz, respectively so that their BFSs remain approximately at the middle of the corresponding frequency ranges. For example, the measured BGSs at three different temperatures of 25°C, 50°C and 75°C for different pump-pulse widths of 10 ns, 15 ns, 30 ns and 100 ns are shown in Fig. 3.

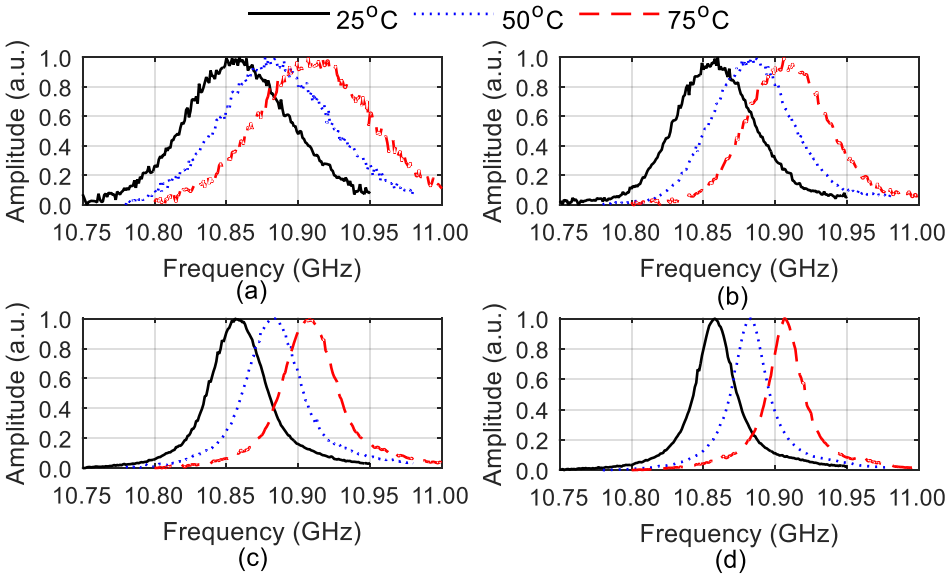

Fig. 3. The measured BGSs at three different temperatures of 25°C, 50°C and 75°C for different pump-pulse widths of (a) 10 ns, (b) 15 ns, (c) 30 ns and (d) 100 ns.

It is observed from Fig. 3 that the BFS (i.e., central frequency) of the measured BGS obtained for given pump-pulse width changes significantly with temperature but remains almost the same at a given temperature for the variation of pump-pulse width. In contrast, the FWHM of the measured BGS obtained for a given pump-pulse width remains almost unchanged with temperature but changes greatly for the variation of pump-pulse width at a given temperature. It is also noticed in Fig. 2 and Fig. 3 that the level of noise in the BGSs obtained using shorter pump-pulse is relatively higher. This is because the measured BGS experiences lower gain due to the lower average power of shorter pump-pulse but it is corrupted by random noise [21,22]. To reduce the level of noise in the measured BGS, it is needed to increase the peak power of the pump-pulses which gives rise to other adverse effects, such as modulation instability and non-local effects [22,23].

4.2 Selection of proper spectrum profile for the measured BGS

For the selection of proper spectrum profile, curve fitting technique is used to fit the measured BGSs. For this, the measured BGSs obtained at three different temperatures of 25°C, 50°C and 75°C each time for different pump-pulse widths ranging from 10 ns to 100 ns are fitted using LCF, GCF and pVCF. For instance, the measured BGSs obtained at 25°C and their fitted BGSs are shown in Fig. 4 for different pump-pulse widths of 10 ns, 15 ns, 30 ns and 100 ns.

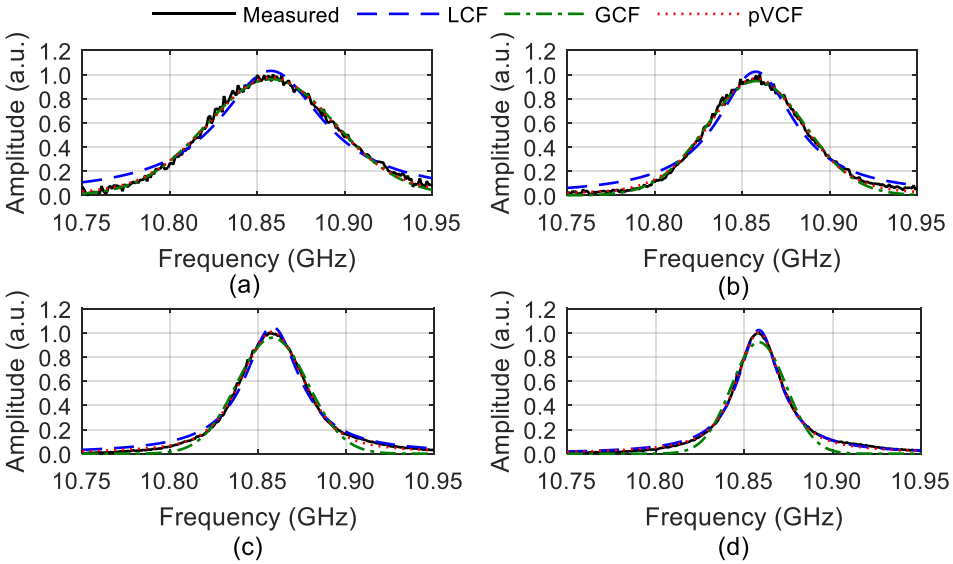

Fig. 4. Measured and fitted BGSs obtained at 25°C for different pump-pulse width of (a) 10 ns, (b) 15 ns, (c) 30 ns and (d) 100 ns.

The measured and fitted BGSs in Fig. 4 at 25°C for four different pump-pulse widths indicate that the BGS obtained using shorter pump-pulse width (e.g. 10 ns) can be well-fitted using GCF, i.e., the shape of the measured BGS is mostly Gaussian as shown in Fig. 4(a). When the width of the pump-pulse increases, the measured BGSs gradually tend to be situated in between Lorentzian and Gaussian profiles as shown Fig. 4(b) and Fig. 4(c) and neither LCF nor GCF can be used accurately to fit them. On the other hand, the shape of the measured BGS obtained for 100 ns is mostly Lorentzian and thus can be well-fitted using LCF as indicated in Fig. 4(d). However, the pVCF

always provides best fitting performances regardless the pump-pulse widths used in the BOTDA experiment to obtain the measured BGSs.

To evaluate the fitting performances of LCF, GCF and pVCF quantitatively, the measured and fitted BGSs are compared in terms of root mean square error (RMSE) and coefficient of determination (R^2). The RMSE for a measured BGS is calculated using the residuals from its fitted curve and the R^2 is calculated to be the square of the correlation between the measured BGS and its fitted curve as given by Eq. (5) and Eq. (6), respectively.

$$RMSE = \sqrt{\frac{\sum_{i=1}^{N}\left[g_m(\upsilon_i) - g_f(\upsilon_i)\right]^2}{N}} \tag{5}$$

$$R^2 = \frac{\left[\sum_{i=1}^{N}\left\{g_m(\upsilon_i) - \mu_m\right\}\left\{g_f(\upsilon_i) - \mu_f\right\}\right]^2}{\sum_{i=1}^{N}\left[g_m(\upsilon_i) - \mu_m\right]^2 \sum_{i=1}^{N}\left[g_f(\upsilon_i) - \mu_f\right]^2} \tag{6}$$

In Eq. (5) and Eq. (6), $g_m(\upsilon_i)$ and $g_f(\upsilon_i)$ represent each of the N data points of the measured and fitted BGSs and, μ_m and μ_f are the mean values of $g_m(\upsilon_i)$ and $g_f(\upsilon_i)$ respectively. A lower value of RMSE indicates better fit. The value of R^2 ranges from 0 to 1 and a value of 1 indicates perfect fit. The RMSE and R^2 values for measured BGSs obtained using different pump-pulse widths at three different temperatures of 25°C, 50°C and 75°C are shown in Fig. 5.

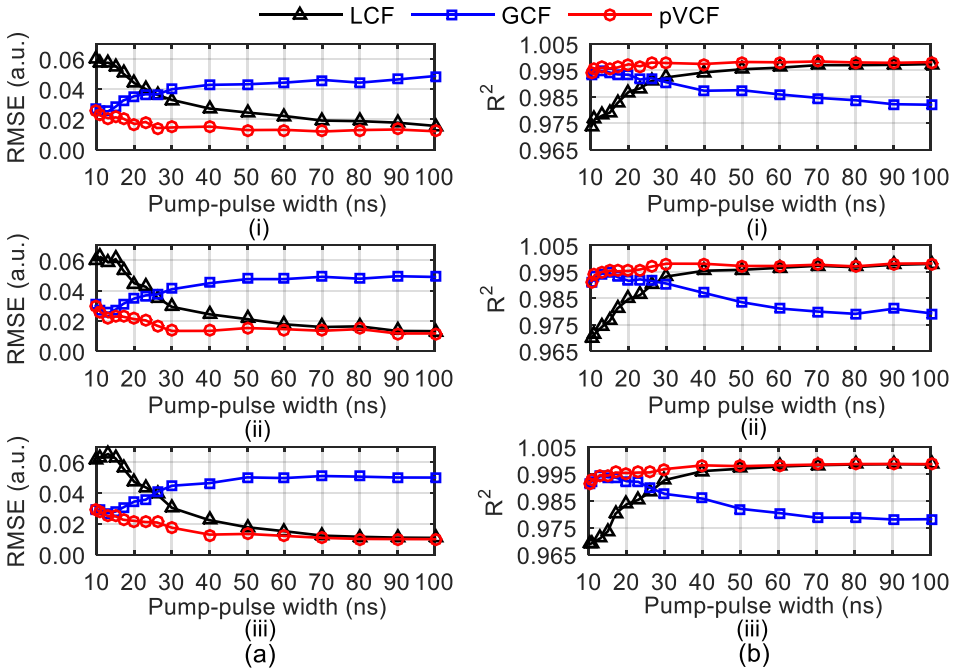

Fig. 5. (a) RMSE and (b) R^2 values in the fitting with different spectrum profiles for measured BGSs obtained at different temperatures of (i) 25°C (ii) 50°C and (iii) 75°C.

The results in Fig. 5 reveal that GCF gives better fitting performance at each of the three different temperatures as compared to LCF for the measured BGSs obtained using shorter pump-pulse. On the other hand, the fitting performance of LCF is better than that of GCF for the measured BGSs obtained using longer pump-pulse. This is because, the shape of measured BGSs obtained using shorter pump-pulse are mostly Gaussian and their shapes diverge from Gaussian to Lorenzian as the pump-pulse width increases. However, the RMSE and R^2 values in Fig. 5 signify that pVCF always gives the minimum RMSE and maximum R^2 values, i.e., best fitting performance as compared to both GCF and LCF for the measured BGSs obtained for all pump-pulse widths at three different temperatures. Thus, the effects of pump-pulse width and temperature on three parameters (i.e., *L*, BFS, and FWHM) of the measured BGSs are analyzed next using pVCF only.

4.3 Effect of pump-pulse width and temperature on the measured BGSs

To analyze the effect of pump-pulse width and temperature, the measured BGSs obtained for a particular pump-pulse width at a particular temperature is fitted by using pVCF. In such fitting process, the measured BGS is fitted with the pseudo-Voigt profile given by Eq. (3) to extract three parameters, i.e., *L*, BFS, and FWHM. The variations of *L*, BFS and FWHM with different pump-pulse widths and temperatures are analyzed next.

To investigate the effects of pump-pulse width and temperature on *L* and FWHM, the measured BGSs obtained at three different temperatures of 25°C, 50°C and 75°C and different pump-pulse widths adopted in this study are fitted using pVCF. The variations of Lorentzian proportion *L* and FWHM of the measured BGSs obtained with different pump-pulse widths at three different temperatures are shown in Fig. 6(a) and Fig. 6(b), respectively.

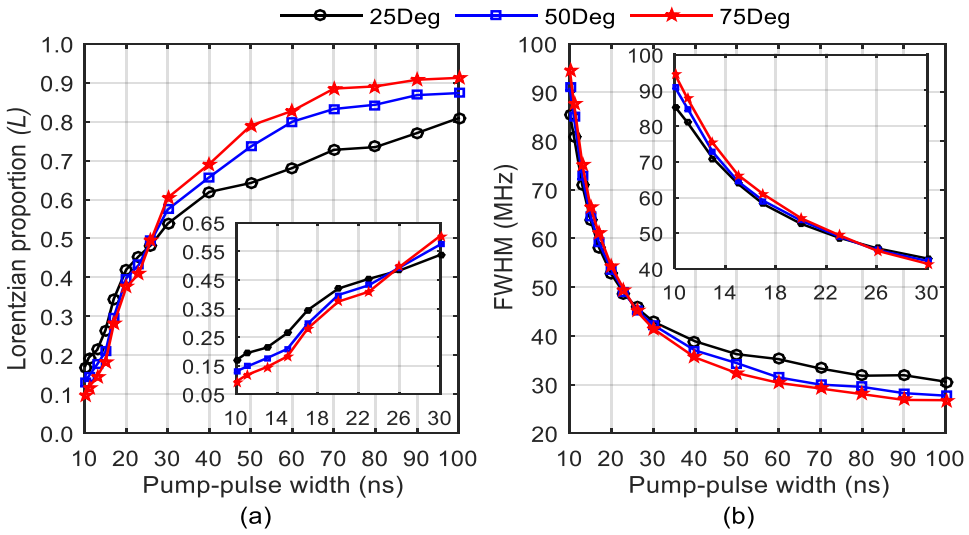

Fig. 6. Variations of (a) Lorentzian proportion, *L* and (b) FWHM of the measured BGSs with different pump-pulse width. [Inset: variation of *L* and FWHM within the pump-pulse width ranging from 10 ns to 30 ns].

It is observed from Fig. 6(a) that *L* values of the measured BGSs obtained for shorter pump-pulses (e.g., < 20 ns) are relatively smaller at each of the three different temperatures, i.e., the measured BGSs are mostly Gaussian. The results also show a gradual increase of *L* values when the measured

BGSs are obtained using longer pump-pulses and the measured BGSs become mostly Lorentzian for pump-pulses longer than 40 ns. The results confirm the gradual change of the shapes of measured BGSs from Gaussian to Lorentzian due to the increase of pump-pulse width. A new phenomenon is also observed from Fig. 6(a) that the *L* values of the measured BGSs obtained at three different temperatures remain almost the same (i.e., *L* = ~0.5) when a characteristic pump-pulse width of ~26 ns is used in the BOTDA setup. For such pump-pulse width, the measured BGSs obtained at three different temperatures of 25°C, 50°C and 75°C have shapes which are situated almost in the middle of a Lorentzian and a Gaussian profiles. For the pump-pulse widths shorter than ~26 ns, the *L* value decreases with temperature. An opposite effect of temperature is found for pump-pulse widths longer than ~26 ns where *L* value increases with temperature. This is because the pump-pulse having a certain minimum width (i.e., characteristic pump-pulse width) is required to fully stimulate the phonons in the FUT and a pump-pulse shorter that such width makes a decrease in the gain of the measured BGSs [24-26]. The variations of FWHM in Fig. 6(b) with pump-pulse width and temperature shows the opposite trends as compared to the variations of Lorentzian proportion *L* in Fig. 6(a). At a particular temperature, FWHM of the measured BGS decreases when longer pump-pulse width is used in the BOTDA setup. For a particular pump-pulse width, the FWHMs of the measured BGSs also show a little change with temperature. However, the FWHMs of the measured BGSs obtained for pump-pulse width shorter than the characteristic pump-pulse width of ~26 ns increases with temperature but decreases for the pump-pulse width longer than such characteristic pump-pulse width. The results in Fig. 6(a) and Fig. 6(b) show an inverse relationship of FWHM with Lorentzian proportion *L*.

The results in Fig. 6(a) show that the *L* values of the measured BGSs increase or decrease with temperature for the pump-pulse width longer or shorter than the characteristic pump-pulse width of ~26 ns. On the contrary, the FWHMs of the measured BGSs increase or decrease with temperature for the pump-pulse width shorter or longer than ~26 ns as shown in Fig. 6(b). To verify the effect of temperature clearly on both sides of the characteristic pump-pulse width, the measured BGSs obtained for two different pump-pulse widths of 20 ns (i.e., < 26 ns) and 70 ns (i.e., > 26 ns) at different temperatures are fitted using pVCF. The results are plotted in Fig. 7.

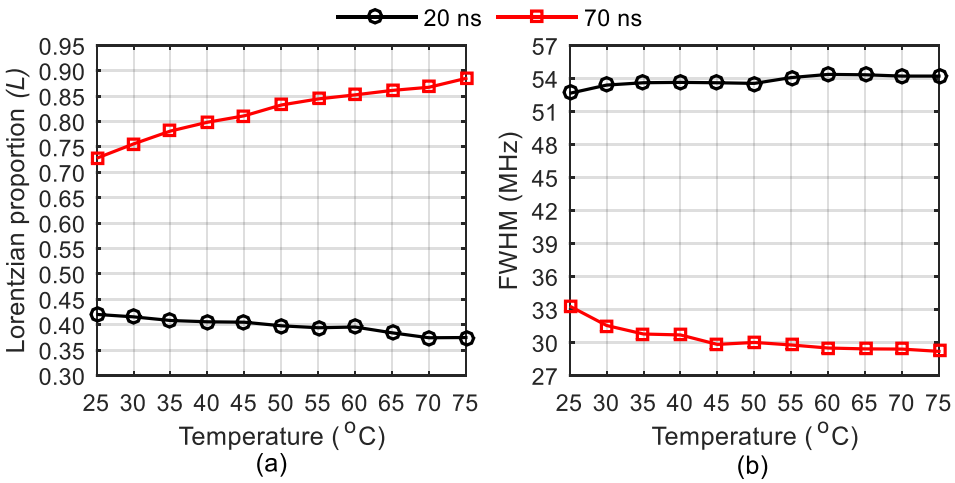

Fig. 7. Variations of (a) Lorentzian proportion, *L* and (b) FWHM of the measured BGSs with temperature.

The results in Fig. 7(a) show a decrease in *L* value with temperature for the measured BGS obtained for pump-pulse width of 20 ns while it is increased for the pump-pulse width of 70 ns. As a result, the FWHM of the measured BGS in Fig. 7(b) increases with temperature for pump-pulse width of 20 ns but decreases with that for the pump-pulse width of 70 ns. The results in Fig. 7 again confirm the opposite effects of temperature on the shape and FWHM of the measured BGSs obtained for pump-pulse width shorter and longer that the characteristic pump-pulse width.

Finally, the effects of pump-pulse width and temperature on the BFS of the measured BGS are analyzed. For the measurement of temperature distributions using the BOTDA sensor, the BFS distributions are first extracted and the BFS-temperature characteristics of the given FUT are then used to determine the temperature distributions along the FUT [3,4]. To study the effects of pump-pulse width and temperature on BFS, the measured BGSs obtained at three different temperatures of 25°C, 50°C and 75°C for different pump-pulse widths and that obtained for two different pump-pulse widths of 20 ns and 70 ns at different temperatures are fitted using pVCF to extract BFSs. The results are shown in Fig. 8.

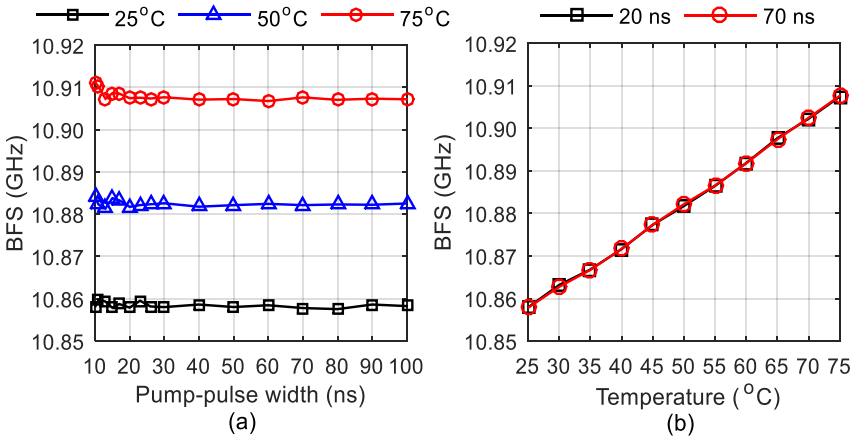

Fig. 8. Variations of BFS of the measured BGSs with (a) pump-pulse width and (b) temperature.

The results in Fig. 8(a) indicate that the BFS of the measured BGS obtained at a given temperature do not vary with pump-pulse width. However, the BFS of the measured BGS obtained for a particular pump-pulse width varies linearly with temperature as shown in Fig. 8(b) and the slope of this linear variation is ~1 MHz/°C which is well supported in literature [4,14]. It is worth mentioning that the little variations of the BFSs at three different temperatures in Fig. 8(a), especially for shorter pump-pulse widths are due to the fact that the levels of noise in the measured BGSs obtained using shorter pump-pulse is relatively higher. This is because the gain of the measured BGS is relatively lower due to the lower average power of shorter pump pulse but the measured BGS is corrupted by random noise.

5. CONCLUSIONS

In this paper, a comprehensive analysis of the effects of pump-pulse width and temperature on the measured BGS obtained from a BOTDA sensor is presented experimentally. Different spectrum profiles are used to fit the measured BGSs obtained for various pump-pulse widths and temperatures. By quantitative analysis, it is confirmed that pseudo-Voigt profile can be efficiently and accurately

used to fit the measured BGSs. The variation of the Lorentzian proportion in pseudo-Voigt profile also validates that the shape of the measured BGS obtained at a given temperature shifts gradually from Gaussian profile to Lorentzian profile when longer pump-pulse width is used in the BOTDA experiment. As a result, the FWHM of the measured BGS also decreases with pump-pulse width. A new phenomenon is also observed in this study which signifies that the variations of spectrum shape and FWHM of the measured BGSs with temperature show an opposite trends for pump-pulse widths shorter and longer than a characteristic pump-pulse width. It is also observed that the BFS of the measured BGS obtained at a given temperature remain constant even if the width of the pump-pulse is varied. However, the variation of BFS with temperature for a given pump-pulse width supports the existing linear BFS-temperature relationship for the FUT. Thus, the analysis performed in this study can be effectively utilized to accurately model different signal processing techniques for extracting temperature distribution using BOTDA sensors.

ACKNOWLEDGEMENT

The author would like to acknowledge the support of PolyU Photonics Research Center at The Hong Kong Polytechnic University for providing the facility of the experiment.

REFERENCES

[1] X. Bao, and L. Chen, Recent progress in distributed fiber optic sensors, Sensors (Basel) **12**(12), 8601-8639 (2012).

[2] X. Liu, B. Jin, Q. Bai, Y. Wang, D. Wang, and Y. Wang, distributed fiber-optic sensors for vibration detection, Sensors, **16**, 1164 (2016).

[3] L. Thévenaz, Brillouin distributed time-domain sensing in optical fibers: state of the art and perspectives, Frontier. Optoelectron. China **3**, 13-21 (2010).

[4] C. A. Galindez-Jamioy, and J. M. Lopez-Higuera, Brillouin distributed fiber sensors: An overview and applications, J. Sensors, **2012**, Article ID 204121, 1-17 (2012).

[5] A. Motil, A. Bergman, and M. Tur, State of the art of Brillouin fiber-optic distributed sensing, Optic. Laser Technol., **78**(A), 81-103 (2016).

[6] A. Minardo, A. Coscetta, L. Zeni, and R. Bernini, High-spatial resolution DPP-BOTDA by real-time balanced detection, IEEE Photonic. Technol. Lett., **26**(12), 1251-1254 (2014).

[7] M. A. Soto, G. Bolognini, and F. D. Pasquale, Optimization of long-range BOTDA sensors with high resolution using first-order bi-directional Raman amplification, Optic. Express, **19**(5), 4444-4457 (2011).

[8] M. Niklès, L. Thévenaz, and P. A. Robert, Brillouin gain spectrum characterization in single-mode optical fibers, J. Lightwave Technol., **15**(10), 1842-1851 (1997).

[9] S. M. Haneef, Z. Yang, L. Thévenaz, D. Venkitesh, and B. Srinivasan, Performance analysis of frequency shift estimation techniques in Brillouin distributed fiber sensors, Optic. Express, **26**(11), 14661-14677 (2018).

[10] M. G. Herráez, K.Y. Song, and L. Thévenaz, Arbitrary-bandwidth Brillouin slow light in optical fibers, Optic. Express, **14**(4), 1395-1400 (2006).

[11] M. Chen, Z. Meng, J. Wang, and W. Chen, Ultra-narrow linewidth measurement based on Voigt profile fitting, Optic. Express, **23**(5), 6803-6808 (2015).

[12] Z. Xu, Zhiniu, and L. Zhao, Key parameter extraction for fiber Brillouin distributed sensors based on the exact model, Sensors, **18**, 1-20 (2018).

[13] X. Bao, A. Brown, M. DeMerchant, and J. Smith, Characterization of the Brillouin-loss spectrum of single-mode fibers by use of very short (<10-ns) pulses, Optic. Lett., **24**(8), 510–512 (1999).

[14] A. K. Azad, F. N. Khan, W. H. Alarashi, N. Guo, A. P. T. Lau, and C. Lu, Temperature extraction in Brillouin optical time-domain analysis sensors using principal component analysis based pattern recognition, Optic. Express, **25**(14), 16534-16549 (2017).

[15] A. K. Azad, L. Wang, N. Guo, H. Y. Tam, and C. Lu, Signal processing using artificial neural network for BOTDA sensor system, Optic. Express., **24**(6), 6769-6782, (2016).
[16] Y. Liang, J. Jiang, Y. Chen, R. Zhu, C. Lu and Z. Wang, Optimized feedforward neural network training for efficient Brillouin frequency shift retrieval in fiber, IEEE Access, **7**, 68034-68042 (2019).
[17] Y. Chang, H. Wu, C. Zhao, L. Shen, S. Fu, and M. Tang, Distributed Brillouin frequency shift extraction via a convolutional neural network, Photonic. Res., **8**(5), 690-697 (2020).
[18] B. Wang, N. Guo, L. Wang, C. Yu and C. Lu, Robust and fast temperature extraction for Brillouin optical time-domain analyzer by using denoising autoencoder-based deep neural networks, IEEE Sensor. J., **20**(7), 3614-3620 (2020).
[19] Z. Xu and L. Zhao, Estimation of error in Brillouin frequency shift in distributed fiber sensor, IEEE Sensor. J., **20**(4), 1829-1837, (2020).
[20] C. Zhang, Y. Yang, A. Li, Application of Levenberg-Marquardt algorithm in the Brillouin spectrum fitting, Proc. SPIE 7129, 7th Int. Sympos. Instrument. Control Technol., 71291Y, (2008).
[21] H. Iribas, J. Mariñelarena, C. Feng, J. Urricelqui, T. Schneider, and A. Loayssa, Effects of pump pulse extinction ratio in Brillouin optical time-domain analysis sensors, Optic. Express, **25**(22), 27896-27912 (2017).
[22] R. Ruiz-Lombera, J. Urricelqui, M. Sagues, J. Mirapeix, J. M. López-Higuera, and A. Loayssa, Overcoming nonlocal effects and Brillouin threshold limitations in Brillouin optical time-domain sensors, IEEE Photonic. J., **7**(6), 6803609 (2015).
[23] M. Alem, M. A. Soto, and L. Thévenaz, Analytical model and experimental verification of the critical power for modulation instability in optical fibers, Optic. Express **23**(23), 29514–29532 (2015).
[24] G.Tong, L. AiQun, S. YongSheng, Z. Biao, L. Yang and Y. NingSheng, Experimental study on strain and deformation monitoring of reinforced concrete structures using PPP-BOTDA, Sci. China Ser. E: Technol. Sci., **52**(10), 2859-2868 (2009).
[25] H. Zhang, and Z. Wu, Performance evaluation of PPP-BOTDA-based distributed optical fiber sensors, I. J. Distributed Sensor Net., **2012**, 1-12 (2012).
[26] H. Su, M. Yang, Z. Wen, Pulse-pre pump Brillouin optical time domain analysis-based method monitoring structural multi-direction strain, Struc. Monitor. Maintenance, **3**(2), 145-155 (2016).